

Learned Satellite Radiometry Modeling from Linear Pass Observations

Kimmy Chang

Space Systems Command (A&AS)

Justin Fletcher

Space Systems Command (A&AS)

ABSTRACT

The reconstruction of a 3D model of a satellite is crucial for space domain awareness. In this paper, we demonstrate novel view synthesis (NVS) of satellites from linear pass observations by combining Neural Radiance Fields Without Known Camera Parameters (NeRF--) with data preprocessing techniques. Our study makes several contributions. Firstly, we demonstrate the efficacy of the Neural Radiance Fields approach for satellite applications, using both synthetic SPEED+ datasets and real satellite images obtained from the 1.6-meter and 3.6-meter Advanced Electro-Optical System (AEOS) telescopes situated at the Air Force Maui Optical and Supercomputing (AMOS) Observatory. Secondly, we show that data preprocessing significantly enhances the performance of NeRF--. Thirdly, we demonstrate that our approach can account for various lighting conditions and lack of camera parameters. Finally, we demonstrate that a 3D model of a satellite can be constructed from only 32 images with limited angular range. We evaluate 16 geometric and photometric transformations, from which we construct a performant data preprocessing pipeline for satellite images. In quantitative analysis, we demonstrate that our approach outperforms existing NeRF models and state-of-the-art NeRF variants in terms of peak signal-to-noise ratio (PSNR) and structural similarity index measure (SSIM) within our application domain. Our study is the first to investigate the impact of data preprocessing on NeRF 3D reconstruction in the context of satellite imaging.

1. INTRODUCTION

The fielding and operation of satellites is inherently risky. Any number of carefully choreographed steps in the deployment process may fail and post-deployment anomalies are not uncommon. Furthermore, the burgeoning population of defense-related satellites poses new and urgent characterization challenges [1]. Distance and illumination conditions conspire to restrict ground-based spatially-extended imaging of satellites to large-aperture telescope systems and high-power radars, the scarcity of which demands information-rich sensing paradigms. In this work, we propose a Novel View Synthesis (NVS) approach that enables the prediction of many views using a single linear pass observation from a ground-based optical sensor using an intermediary learned radiance field representation.

3D satellite models enable owners and operators to diagnose satellite configuration issues, assess damage, and determine orientation. A model of a previously unseen satellite can aid in the understanding of that satellite's intended roles and potential uses within its orbital regime. In this paper, we investigate the feasibility of combining Neural Radiance Fields (NeRF) and data preprocessing techniques to create such models using both synthetic and real satellite images obtained from linear pass observations.

In keeping with our ground-based imaging application, our study does not restrict the evaluation dataset to ideal (i.e., photometric) conditions. Rather, we explore satellite images that exhibit noisy and variable lighting conditions, and we also limit the angular diversity and number of images of each satellite. Furthermore, we eliminate the assumption of known camera parameters, which is a departure from the standard assumptions in this field [9, 6, 8, 2].

The rest of this paper is organized as follows. Section II elaborates on this "less than ideal" dataset condition. Section III provides a detailed description of our dataset, while Section IV outlines our general approach and model. In Section V, we introduce our method, which comprises several components, including metrics, geometric and photometric transformations, baseline, and model choice. Section VI presents a summary of our results and analysis, while Section VII describes the limitations of our work. Finally, in Section VIII, we conclude our research by discussing potential extensions of our work for future studies.

2. RELATED WORKS

This work lies at the intersection of NeRF applications and satellite radiometric and geometric modeling. This section describes relevant work in each domain.

2.1 Satellite Model Prediction

Prior work has established the efficacy of NeRF [7, 4] and Generative Radiance Fields (GRAF) [14] on images of spacecraft with impressive results. Of particular relevance is *Mergy et. al.*, which demonstrated that while both NeRF and GRAF are able to learn 3D differentiable representations of spacecraft with distinct geometry, NeRF generally achieves better performance [7]. *Lucas et. al.* found NeRF to be the most superior method for the discoverability of 3D object structure from passive observations of objects¹ [4]. Nevertheless, both studies were limited to synthetic dataset results, sufficient view diversity, and ideal conditions (limited lighting variability and occlusions).

2.2 3D Reconstruction from NeRF

The NeRF method, proposed by *Mildenhall et al.*, generates high fidelity 3D reconstructions from sets of synthetic and real images [9] but also entails several prerequisites that are not met by electro-optical images of satellite. The NeRF approach (1) requires known camera parameters for each image, (2) assumes that the scene was stable geometrically, materially, and photometrically, (3) performs well only for low-noise images, (4) needs many input views, and (5) requires extensive training. Overcoming these limitations is vital to the creation of a successful NeRF model for satellite modeling.

Several approaches attempt to address some of these limitations during the NeRF training process. For example, *Wang et al.*'s [16] Neural Radiance Fields Without Known Camera Parameters (NeRF--) achieved comparable results by optimizing camera parameters as learnable parameters in the training process. Similarly, *Deng et al.*'s [2] DS-NeRF utilized “free” sparse representations from structure-from-motion for depth supervision, reducing convergence time and the number of training images required. However, the DS-NeRF method requires knowledge of 3D keypoints.

Noisy and variable lighting conditions are prominent challenges in 3D reconstruction from 2D images [6, 8]. *Martin et al.*'s [6] approach of using Generative Latent Optimization and decomposing image elements into static and transient components enabled NeRF in the Wild (NeRF-W) to account for image-specific variations such as exposure and lighting. Nonetheless, NeRF-W was sensitive to camera calibration errors and was unable to render areas of the scene that were rarely observed during training. NeRF in the Dark (RawNeRF) [8] addressed these limitations by directly supervising on noisy raw input images, transforming it into a multi-image denoiser and enabling the reconstruction of dimly lit environments through the adaptation of high dynamic range (HDR) images as input.

Table 1 summarizes the attributes of interest for the NeRF model and its variants.

Table 1: Comparison of NeRF and NeRF variants

Model	Model Attributes		
	No COLMAP ¹	Variable Light/Noise	Sparse Image Set
NeRF	×	×	×
NeRF--	✓	×	✓
NeRF-W	×	✓	×
DS-NeRF	×	×	✓
RawNeRF	×	✓	×

¹This means that camera parameters do not need to be known for training.

2.3 Data Preprocessing

Prior literature has shown that preprocessing techniques can enhance the performance of 3D reconstruction models. For instance, *Gaiani et al.* [3] have demonstrated the benefits of preprocessing images based on color enhancement, image denoising, color-to-gray conversion, and image content enrichment prior to training. Furthermore, *Taylor et al.* [15] have explored the effectiveness of various geometric and photometric transformations, such as cropping, rotating,

¹In contrast to a deformable mesh implementation

**DISTRIBUTION A. Approved for public release: distribution is unlimited.
Public Affairs release approval #AFRL-2023-378**

and shifting pixel values based on pre-defined heuristics on convolutional neural networks. In a similar vein, *Lv et al.* [5] have demonstrated the effectiveness of data augmentation methods for face recognition from a limited set of images.

3. DATA

The present research utilizes a diverse set of data sources, comprising the synthetic and sunlamp subsets of the SPEED+ [12] dataset and real satellite images gathered through observations using a 1.6-meter and a 3.6-meter telescope. The synthetic dataset from SPEED+ encapsulates the scenario of ideal lighting conditions, while the sunlamp subset encompasses challenging sources of illumination, such as corner cases, stray light, and shadowing, amongst other visual effects. In particular, the sunlight dataset emulates direct, high intensity homogeneous light emanating from the Sun. As is evident in Fig. 1, solar illumination obscures fine details within certain geometries, a challenge to this work even in high signal observations. Notably, each model in this research is trained on a set of 32 images.

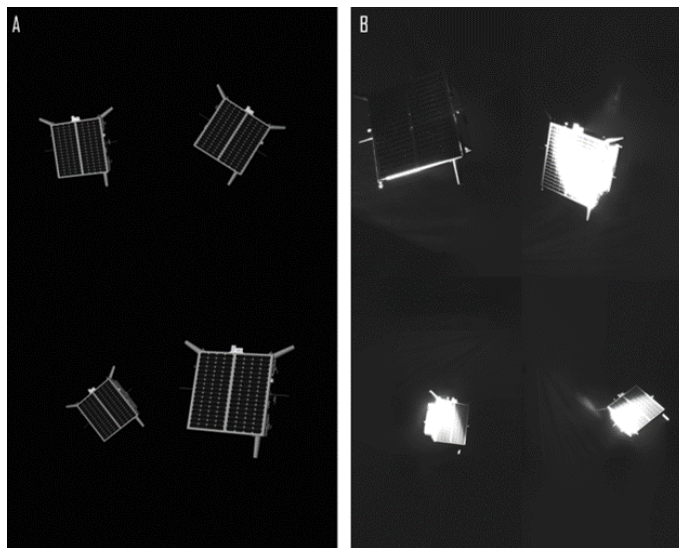


Fig. 1: A. Synthetic images. B. Sunlamp images. [12]

4. APPROACH AND MODEL

In order to achieve 3D reconstructions from 2D satellite images, we propose an approach that combines Neural Radiance Fields with data preprocessing techniques. In this study, we will assess the effectiveness of two geometric transformations and fourteen photometric transformations on the quality of the reconstructions. Additionally, we investigate the combination of these preprocessing techniques for the 3D reconstruction of satellites.

4.1 NeRF

NeRF expresses a complex scene² with a continuous function as shown in Eq. (1).

$$L_o, \sigma = f(x, y, z, \theta, \phi) \quad (1)$$

where (x, y, z) is a spatial location, (θ, ϕ) is the viewing direction, L_o and σ are the emitted radiance and volume density at (x, y, z) respectively.

To synthesize a scene from an arbitrary viewpoint, we can estimate the corresponding pixel values by querying positions along a specific camera view direction defined by the angles θ and ϕ and the position coordinates (x, y, z) . By synthesizing the scene in this way, we can create a representation of the 3D environment from different perspectives.

²A “complex scene” in the context of 3D reconstruction poses one or more of the following challenges: fine-scale surface details, variable lighting conditions, occlusions, and/or significant geometric complexity.

4.1.1 Volume Rendering

Radiance emitted from a point source is partially absorbed by the medium through which it propagates [13] as shown in Fig. 2.

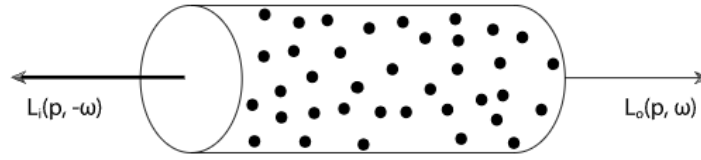


Fig. 2: Volume Absorption: $p = (x, y, z)$ is a spatial location and ω is a solid angle, L_i is the incident radiance, and L_o is the output radiance.

Given that density of a volume is σ , within a short distance, dt , we have

$$\begin{aligned} L_o - L_i &= -\sigma L_i dt \\ dL_o &= -\sigma L_i dt \end{aligned} \quad (2)$$

According to Eq. (2), if the light travels a distance t , the remaining portion is

$$T(t) = \exp\left(-\int_0^t \sigma dt\right) \quad (3)$$

Therefore, the value of a pixel at distance o can be estimated by integrating the radiance at position $p(t) = o + dt$ through the view ray d from the near plane to far plane of the viewing frustum.

$$C(o, d) = \int_{t_{\text{near}}}^{t_{\text{far}}} T(t) \sigma(p(t)) L_o(p(t)) dt \quad (4)$$

The numerical expression of Eq. (4) is shown below [10].

$$\begin{aligned} \hat{C} &= \sum_{i=0}^N T_i \alpha_i l_i \quad \text{where} \\ T_i &= \exp\left(-\sum_{j=1}^{i-1} \sigma_j \delta_j\right) \\ \alpha_i &= 1 - \exp(-\sigma_i \delta_i) \\ \delta_i &= t_{i+1} - t_i \end{aligned}$$

The quantities l_i and σ_i can be deduced by probing the function $f(o + d(t_i), d)$. This, in turn, enables us to generate a synthesized representation of the scene.

4.1.2 NeRF Model Architecture: Multi-Layer Perceptron

We adopt the architecture proposed in [9] in order to generate the $W \times H \times N$ query points where W, H, N correspond to the width and height of the image as well as the number of samples along the view ray, respectively. The architecture uses a fully connected neural network with 8 hidden layers, each containing 256 neurons, followed by a ReLU activation layer (see Fig. 3).

Park et. al [11] suggested that inserting input in the middle layer can enhance learning. Thus, in our approach, we concatenate the input with the output of the fourth layer, which serves as the input of the fifth layer. We employ ReLU

DISTRIBUTION A. Approved for public release: distribution is unlimited.
Public Affairs release approval #AFRL-2023-378

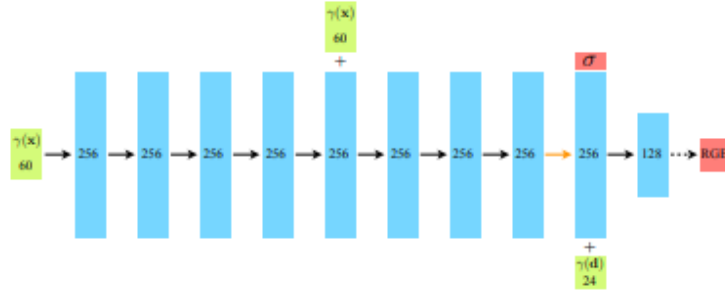


Fig. 3: Structure of MLP

activation to generate the σ value and sigmoid activation to produce radiance. To quantify the discrepancy between the predicted and true images, we use the Frobenius norm of the distortion, as shown in Eq. (5).

$$E = \sqrt{\sum_{w=1}^W \sum_{h=1}^H \|C_{wh}^{\hat{}} - C_{wh}\|} \quad (5)$$

4.2 Geometric and Photometric Transformation

In image processing, data augmentation techniques can be separated into geometric and photometric transformations. Geometric transformations change the image geometry by modifying the pixel positions, while photometric transformations alter the image's channels by shifting pixel colors to new values. Notably, the dataset used in this study comprises single-channel data, where each sample represents grayscale information rather than multiple color channels.

5. METHODS

5.1 Metrics

We employ both qualitative and quantitative evaluation to assess the efficacy of our approach. For qualitative evaluation, we visually inspect the quality of the novel views synthesized by our method. For quantitative evaluation, we use two standard performance metrics: peak signal-to-noise ratio (PSNR) and structural similarity index measure (SSIM). PSNR, given by the equation below, measures the average amount of noise present in the reconstructed images relative to the original images:

$$10 \log_{10} \left(\frac{(L-1)^2}{\text{MSE}} \right)$$

Here, L represents the number of maximum possible intensity levels in an image, and MSE is the mean squared error. SSIM, on the other hand, evaluates the similarity between the reconstructed and original images by accounting for their luminance, contrast, and structure. It is computed as follows:

$$\text{SSIM}(x,y) = \frac{(2\mu_x\mu_y + c_1)(2\sigma_{xy} + c_2)}{(\mu_x^2 + \mu_y^2 + c_1)(\sigma_x^2 + \sigma_y^2 + c_2)}$$

where μ_x, μ_y and σ_x^2, σ_y^2 are the averages and variances of x, y , σ_{xy} is the covariance of x and y , and c_1 and c_2 are variables that stabilize the division with weak denominator. SSIM is designed to better reflect human visual perception than PSNR.

We will use both PSNR and SSIM to quantitatively evaluate the performance of our approach. While PSNR is better suited for assessing the quality of noisy images, SSIM is more comprehensive as it takes into account various aspects of image quality.

**DISTRIBUTION A. Approved for public release: distribution is unlimited.
Public Affairs release approval #AFRL-2023-378**

5.2 Geometric and Photometric Transformation

In the context of 3D satellite reconstruction, we investigate various geometric and photometric transformations, including minimal rotation, crop, center, and resize for geometric transformations, and denoise, exposure control, edge enhance, negative transform, sharpen, smooth, contrast stretch, log transform, mode filter, min filter, max filter, median filter, gaussian area blur, and pepper noise for photometric transformations. In the following section, we develop a combination of data augmentation techniques for the purpose of satellite 3D reconstruction.

For visual demonstration, we provide the effects of these transformations on the synthetic and sunlamp subsets of SPEED+ analyzed in this study, which can be seen in Fig. 4 and Fig. 5, respectively.

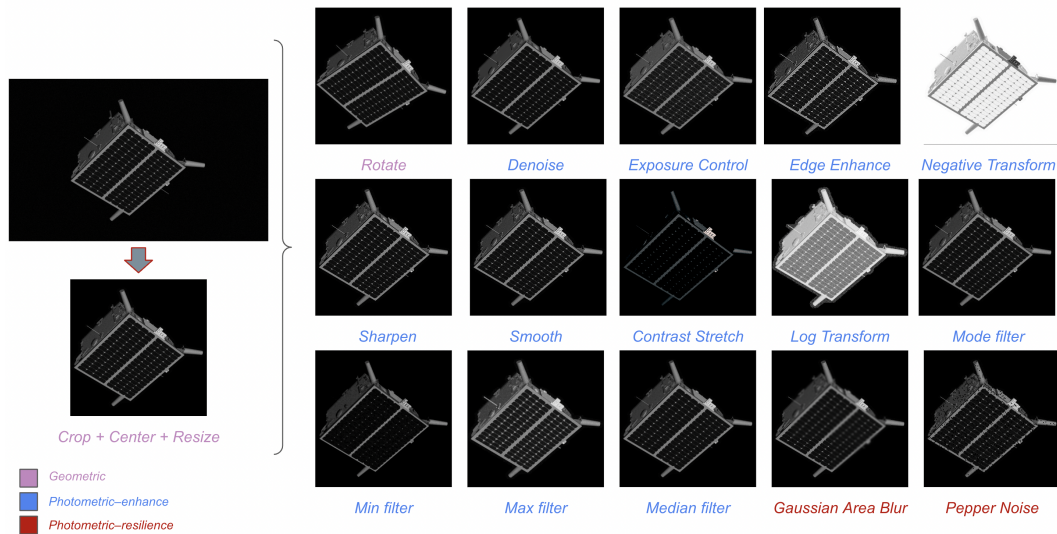


Fig. 4: Synthetic

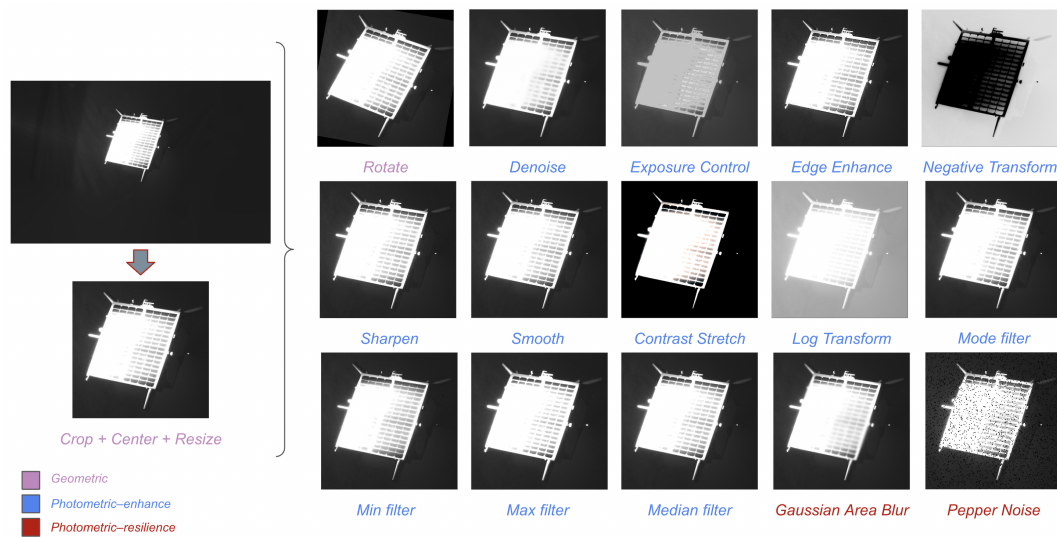


Fig. 5: Sunlamp

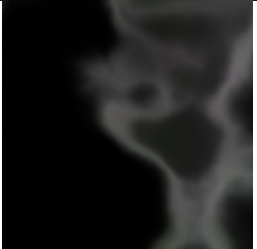
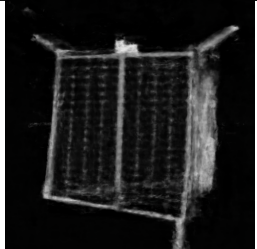

5.3 Baseline Model Performance

We evaluate three different NeRF models as potential baseline models: NeRF, NeRF--, and NeRF-W. While potentially suitable for satellite imaging applications, RawNeRF requires HDR images³ and DS-NeRF requires 3D keypoints, neither of which are available in our datasets.

³While our real dataset includes RAW 16-bit images which would fulfill the HDR requirement, the SPEED+ dataset used to test the majority of our methods is not HDR.

**DISTRIBUTION A. Approved for public release: distribution is unlimited.
Public Affairs release approval #AFRL-2023-378**

In Table 2 we present novel views generated by applying each candidate NeRF model to the a sample from the SPEED+ dataset. Prior to applying the NeRF models, all images were subjected to standard pre-processing techniques such as centering, cropping, and resizing. The novel views in Table 2 are generated from 64-image datasets since COLMAP (prerequisite to NeRF and NeRF-W) failed to converge for lower image numbers.

Model	NeRF	NeRF--	NeRF-W ¹
Novel View Ex.			

¹The novel view is a white image.

Table 2: Baseline Model Results

Of our baseline models, only NeRF-- produced performant novel views. This may be attributed to the inferior quality of COLMAP pose estimations, which is a prerequisite for all models except NeRF--. We therefore assume that NeRF-- may have implicitly compensated for such imprecise poses by exploiting the dataset’s inherent structure.

NeRF-- is based on two assumptions: (1) all images are captured in a forward-facing setup with a certain amount of rotation and translation, and (2) all images are captured with the same intrinsic parameters. The optimization problem for NeRF-- can be expressed as:

$$\Theta, \Pi = \arg \min_{\Theta, \Pi} \mathcal{L}(\hat{\mathcal{I}}, \hat{\Pi} | \mathcal{I})$$

where Π denotes the camera parameters. During the training process, a set of pixels is rendered for each input image, and the reconstruction loss between the rendered colors and ground-truth colors is minimized for the pixels. The entire pipeline is differentiable, allowing for joint optimization of NeRF and camera parameters by minimizing the reconstruction loss. Notably, this approach enables the successful reconstruction of complex 3D scenes with minimal input information.

6. RESULTS AND ANALYSIS

With our baseline established, we now turn to task of adapting NeRF models to NVS for satellite images. Our analysis begins with an overview of our selected geometric and photometric transformations and concludes with the application of the complete techniques to real data.

6.1 Geometric and Photometric Transformations

In this study, we establish a control group comprising geometric and photometric transformations. Specifically, we observe that in order for NeRF—a neural radiance field algorithm—to succeed, cropping, centering, and resizing the original images is necessary. When input images are not cropped and centered on the satellite object, only the black background is recovered in the 3D reconstruction. However, by applying the aforementioned transformations, we observe immediate improvements in novel views, as evidenced by Fig. 6. We present quantitative measures of the performance improvements in Table 3, which includes the peak signal-to-noise ratio (PSNR) and structural similarity index measure (SSIM). The resolution of the control group images is (512, 512), while the original resolution is (1960, 920).

Subsequently, we examine the effects of individual geometric and photometric transformations on the performance of our preprocessing pipeline. The outcomes of our investigation, presented in Table 4, reveal that only two transformations, namely median filter and Gaussian area blur, led to improvements in peak signal-to-noise ratio (PSNR) and structural similarity index measure (SSIM) for both the synthetic and sunlamp datasets. In contrast, transforms such as min filter and log transform led to significant increases in PSNR and SSIM for one dataset and decreases for the other dataset, and were therefore not deemed suitable for our robust preprocessing pipeline.

**DISTRIBUTION A. Approved for public release: distribution is unlimited.
Public Affairs release approval #AFRL-2023-378**

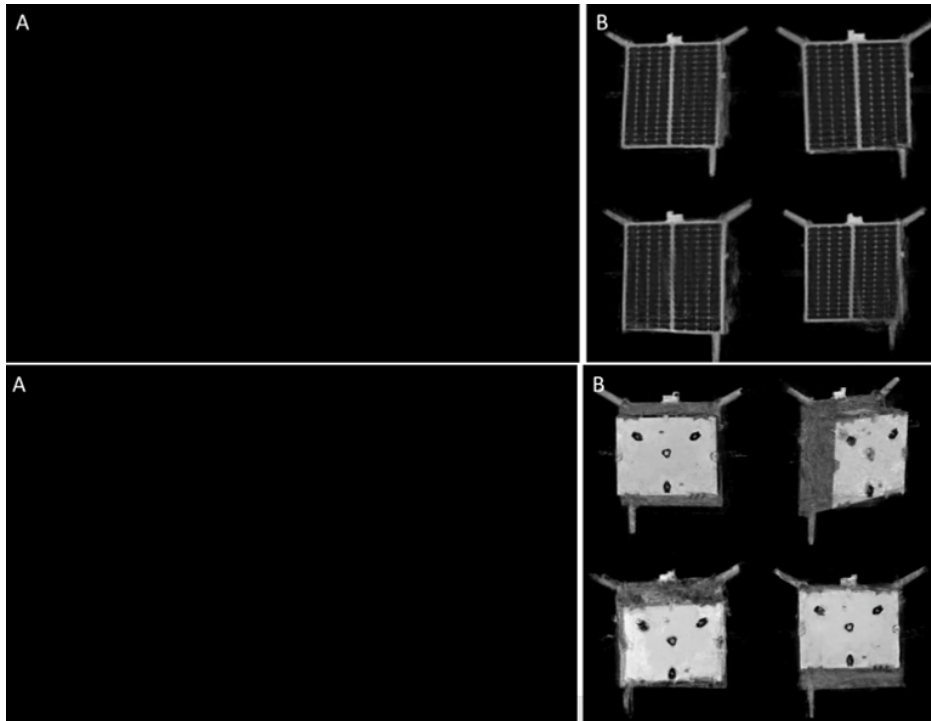


Fig. 6: The original dataset images had novel views that only retrieved the background of images (A). However, after the images underwent crop + center + resize, we were able to recover the following novel views (B).

Table 3: Raw v. Crop, Center, Resize

Dataset	PSNR	SSIM
Original – Top of Satellite	22.536	0.367
Control – Top of Satellite	26.662	0.932
Original – Bottom of Satellite	14.671	0.226
Control – Bottom of Satellite	27.545	0.987

Notably, our analysis demonstrates that rotate, max filter, median filter, denoise, and Gaussian area blur were all effective transformations for improving the performance of our preprocessing pipeline across both datasets. However, given that rotate augmentation led to minimal improvements and greatly increased model training time due to tripling the number of images, we opted not to use this transformation in our final pipeline.

To choose between max and median filter, we examined a subset of novel views for each filter. As illustrated in Figs. 7 and 8, while max filter resulted in lower PSNR and SSIM values, it produced subjectively superior qualitative results for both datasets. For example, with the synthetic subset, the sides of the satellite were not cut off, and with the sunlamp dataset, the square shape of the solar panel top was preserved considerably better. As a result, we combined max filter, denoise, and Gaussian area blur in our final preprocessing pipeline.

The results of various combinations of denoise, max filter, and Gaussian area blur for the synthetic and sunlamp datasets are presented in Table 5. Based on the outcomes, we selected denoise + Gaussian area blur, max filter + denoise + Gaussian area blur, and Gaussian area blur + max filter + denoise as the three combinations to compare the novel views. Our analysis indicates that denoise + Gaussian area blur provided the best overall visual novel views. Therefore, we recommend utilizing denoise + Gaussian area blur in conjunction with the original crop + center + resize as the optimal data preprocessing pipeline for satellite 3D reconstruction. In the subsequent sections, we employ this preprocessing pipeline.

Visuals of the control and denoise + Gaussian area blur for the synthetic and sunlamp datasets are presented in Fig. 9

**DISTRIBUTION A. Approved for public release: distribution is unlimited.
Public Affairs release approval #AFRL-2023-378**

PSNR and SSIM Values for Single Transformation				
Transformation	Synthetic		Sunlamp	
	PSNR	SSIM	PSNR	SSIM
Control	26.662	0.932	23.080	0.965
Rotate	27.412	0.944	22.949	0.965
Min Filter	17.774	0.075	25.625	0.972
Max Filter	26.387	0.947	23.269	0.972
Mode Filter	26.742	0.934	22.351	0.957
Median Filter	28.090	0.949	23.356	0.966
Contrast Stretch	20.120	0.350	20.144	0.935
Smooth	24.493	0.893	21.827	0.951
Exposure	26.142	0.931	25.651	0.962
Log Transform	19.397	0.863	28.654*	0.967
Negative Transform	23.848	0.900	21.799	0.950
Sharpen	24.493	0.892	21.827	0.951
Edge Enhance	19.709	0.914	20.473	0.793
Denoise	26.728	0.932	23.139	0.963
Gaussian Area Blur	30.241*	0.966*	26.014	0.980*
Pepper Noise	24.327	0.875	17.091	0.873

Table 4: Geometric and Photometric Transformation Results

and Fig. 10, respectively. It is evident from these figures that the novel views obtained from the proposed preprocessing pipeline conform more closely to the expected square solar panel shape and exhibit minimal artifacts.

PSNR and SSIM Values for Multiple Transformations				
Transformation	Synthetic		Sunlamp	
	PSNR	SSIM	PSNR	SSIM
<i>Denoise</i>	26.728	0.932	23.139	0.963
<i>Max Filter</i>	26.387	0.947	23.269	0.972
<i>Blur</i>	30.241	0.966	26.014	0.980
Denoise, Max Filter	26.791	0.951	22.472	0.965
Denoise, Max Filter, Blur	29.355	0.970	26.776	0.987
Denoise, Blur	30.605*	0.969	27.351	0.986
Denoise, Blur, Max Filter	29.226	0.966	26.238	0.983
Max Filter, Denoise	26.703	0.950	23.289	0.972
Max Filter, Denoise, Blur	30.130	0.976*	25.876	0.985
Max Filter, Blur	28.497	0.964	25.524	0.984
Max Filter, Blur + Denoise	29.598	0.972	26.258	0.985
Blur, Denoise	30.582	0.970	25.934	0.980
Blur, Denoise, Max Filter	28.951	0.964	26.638	0.985
Blur, Max Filter	29.723	0.969	25.950	0.983
Blur, Max Filter, Denoise	30.129	0.973	27.830*	0.988*

Table 5: Geometric and Photometric Transformation Results

6.2 Real Data

In this section, we extend the application of our work on the SPEED+ dataset to real-world data by investigating the performance of NeRF-- with data preprocessing for linear pass satellite images. The linear pass satellite images analyzed in this study are obtained from a 1.6 meter telescope and a 3.6 meter telescope, and two satellites are examined for each telescope. Information on the satellites can be found in Table 6.

**DISTRIBUTION A. Approved for public release: distribution is unlimited.
Public Affairs release approval #AFRL-2023-378**

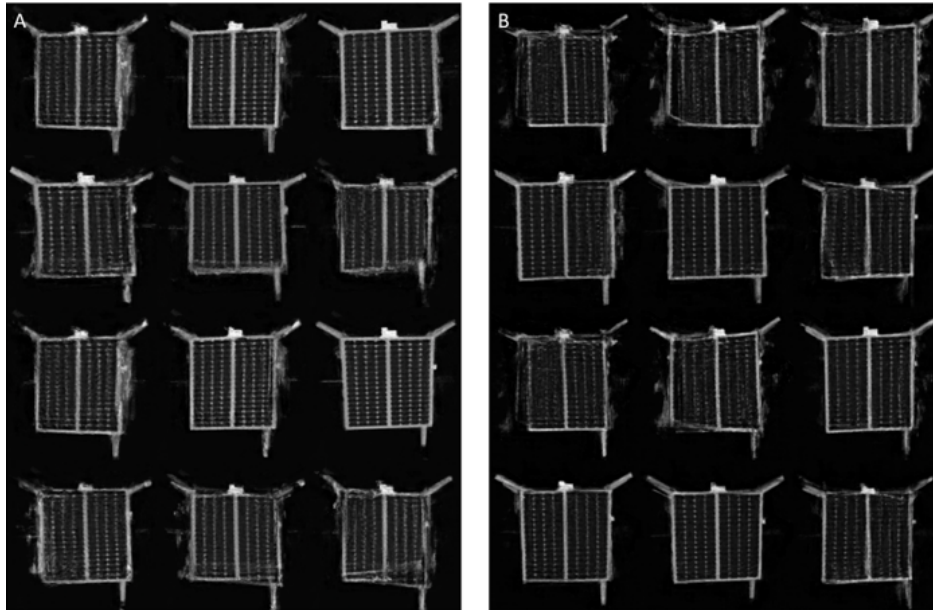


Fig. 7: Novel Views of Synthetic. A - Max Filter. B - Median Filter.

	1.6m AMOS		3.6m AEOS	
	A	B	A	B
<i>Satellite Name</i>	NOAA 13	COSMOS 1606	RESURS O1	SPOT 2
<i>Sensor HFOV/VFOV</i>	25.6481/25.6481	25.6481/25.6481	25.6481/25.6481	25.6481/25.6481
<i>Satellite Z Position</i>	2982195	2872251	3439306	2831563
<i>Timestamp</i>	57967.2933	57971.2588	59697.2840	59697.2820

Table 6: Satellite Details

6.2.1 1.6 meter

The application of data preprocessing to the linear pass satellite images obtained from the 1.6 meter telescope resulted in improved PSNR and SSIM values for both satellites, as indicated in Table 7 and depicted in Figs. 11 and 12. Despite these improvements, the quality and rotational diversity of both satellites are limited, as illustrated in Fig. 13. Specifically, NOAA 13 exhibits minimal changes in its novel views, while COSMOS 1606 demonstrates nearly no variation in its novel views. This observation is further supported by the depth maps depicted in Fig. 14, which indicate that, even with data preprocessing, NeRF-- is unable to effectively learn the 3D characteristics of the satellites.

Table 7: 1.6 meter Satellite Results

Dataset	PSNR	SSIM
NOAA 13 – Control	16.785	0.167
NOAA 13 – Denoise + Blur	39.850	0.995
COSMOS 1606 – Control	35.019	0.987
COSMOS 1606 – Denoise + Blur	39.620	0.995

6.2.2 3.6 meter

In line with our previous experiment on linear pass satellite images from the 1.6 meter telescope, we extend our study to analyze the performance of NeRF-- with data preprocessing on linear pass satellite images captured from a 3.6 meter telescope. As with the previous experiment, we investigate two distinct satellites (RESURS O1 and SPOT 2)

**DISTRIBUTION A. Approved for public release: distribution is unlimited.
Public Affairs release approval #AFRL-2023-378**

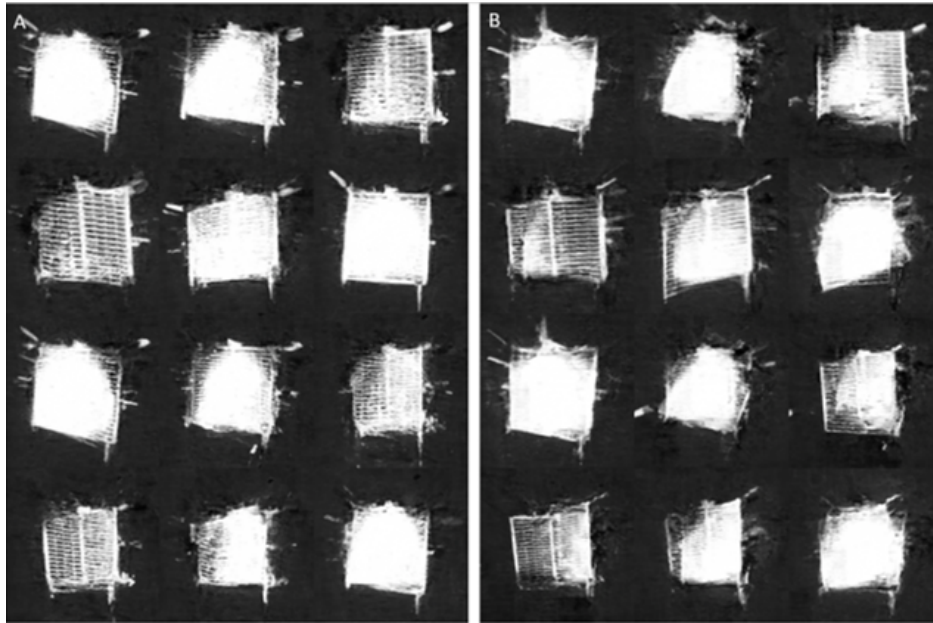


Fig. 8: Novel Views of Sunlamp. A - Max Filter. B - Median Filter.

and assess the impact of data preprocessing on their 3D reconstruction.

Consistent with our previous findings, data preprocessing of the images from the 3.6 meter telescope led to higher PSNR and SSIM values for both satellites, as depicted in Table 8. Moreover, the quality and rotational diversity of both satellites notably improved following data preprocessing, as demonstrated in Fig. 15. Notably, RESURS O1 exhibits clear rotation of the satellite body over the novel views.

To further evaluate the effectiveness of data preprocessing in improving the 3D reconstruction of the satellites, we also assessed the depth maps for both satellites. As shown in Fig. 16, the depth maps demonstrate that the model has learned the 3D properties of the satellites to a greater extent following data preprocessing. Overall, our results suggest that data preprocessing is a crucial step in achieving improved 3D reconstruction of linear pass satellite images from the 3.6 meter telescope.

Table 8: 3.6 meter Satellite Results

Dataset	PSNR	SSIM
RESURS O1 – Control	37.853	0.996
RESURS O1 – Denoise + Blur	40.265	0.997
SPOT 2 – Control	32.064	0.978
SPOT 2 – Denoise + Blur	36.331	0.991

7. LIMITATIONS

The current application has a significant drawback as it can only handle forward-facing scenes, similar to the NeRF--method, and may fail with camera motions having rotation perturbations exceeding $\pm 20^\circ$. As a consequence, spherical datasets cannot be processed by the system, and this limitation may adversely affect non-linear passes. However, for linear passes where rotation perturbations are restricted, this constraint is not an issue.

Moreover, the restoration capabilities of geometric and photometric transformations used in this work have certain limitations. In the future, it will be worthwhile to investigate more common but costly image restoration techniques to overcome these limitations.

**DISTRIBUTION A. Approved for public release: distribution is unlimited.
Public Affairs release approval #AFRL-2023-378**

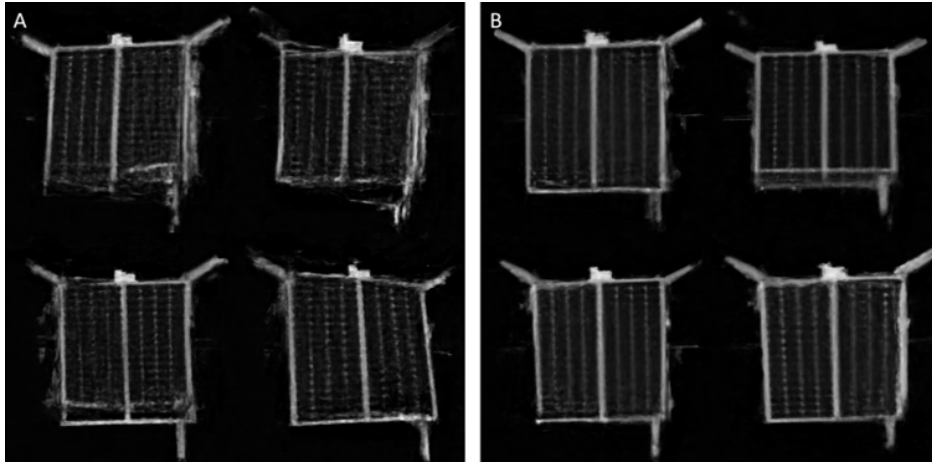


Fig. 9: Novel Views of the Synthetic subset exhibit that Denoise + Blur (B) enhances visual quality and improves fidelity in contrast to the Control (A).

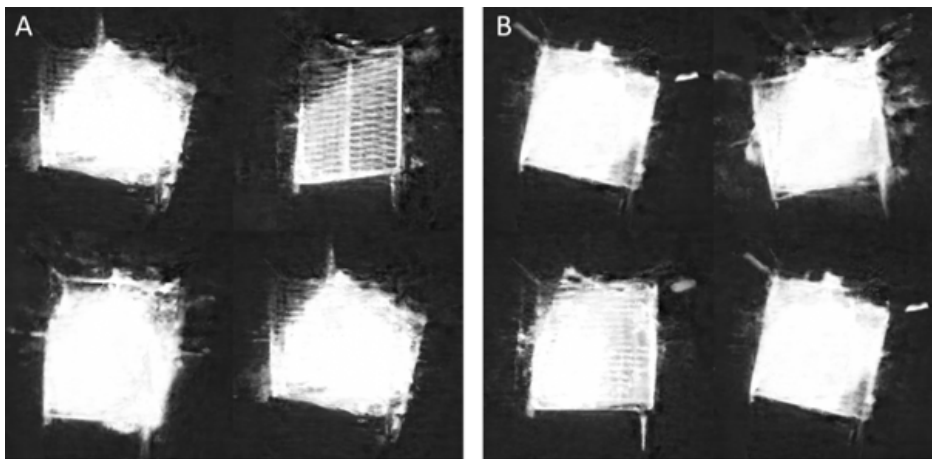


Fig. 10: Novel Views of the Sunlamp subset exhibit that Denoise + Blur (B) enhances visual quality and improves fidelity in contrast to the Control (A).

8. CONCLUSION

We have demonstrated the potential of neural radiance fields (NeRF) methods for 3D satellite radiance modeling. However, the quality of the reconstruction heavily relies on factors such as the number of images, diversity of angular rotation, and lighting/noise conditions. Future work may reduce the impact of these limitations by implementing data preprocessing techniques. Fig. 15 showcases the promise of our approach. Future research will focus on enhancing the quality of images prior to modeling through the application of advanced image restoration methods such as super resolution and image matting.

9. ACKNOWLEDGEMENTS

The authors would like to thank the 15th Space Surveillance Squadron for access to AEOS data. The views and conclusions contained in this document are those of the authors and should not be interpreted as representing the official policies, either expressed or implied, of the United States Air Force or the U.S. Government.

REFERENCES

- [1] Defense Intelligence Agency. 2022 challenges to security in space. Technical report, 2022.

**DISTRIBUTION A. Approved for public release: distribution is unlimited.
Public Affairs release approval #AFRL-2023-378**

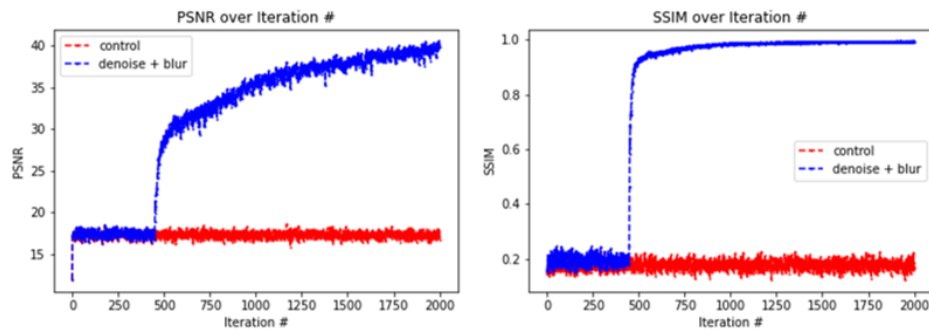


Fig. 11: PSNR and SSIM graphs of NOAA 13.

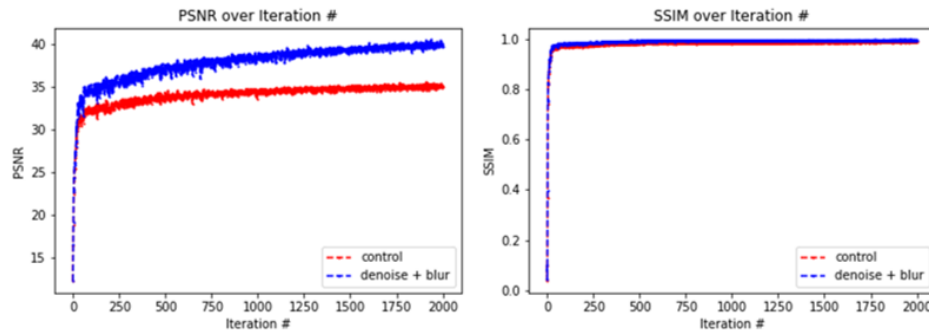


Fig. 12: PSNR and SSIM graphs of COSMOS 1606.

- [2] Kangle Deng, Andrew Liu, Jun-Yan Zhu, and Deva Ramanan. Depth-supervised nerf: Fewer views and faster training for free. *CVPR*, 2022.
- [3] Marco Gaiani, Fabio Remondino, Fabrizio I. Apollonio, and Andrea Ballabeni. An advanced pre-processing pipeline to improve automated photogrammetric reconstructions of architectural scenes. *MDPI, Multidisciplinary Digital Publishing Institute*, 2016.
- [4] Jacob Lucas, Trent Kyono, Julia Yang, and Justin Fletcher. Discovering 3-d structure of leo objects. *AMOS*, 2021.
- [5] Jiang-Jing Lv, Xiao-Hu Shao, Jia-Shui Huang, Xiang-Dong Zhou, and Xi Zhou. Data augmentation for face recognition. *Neurocomputing*, 2017.
- [6] Ricardo Martin-Brualla, Noha Radwan, Mehdi S. M. Sajjadi, Jonathan T. Barron, Alexey Dosovitskiy, and Daniel Duckworth. Nerf in the wild: Neural radiance fields for unconstrained photo. *CVPR*, 2021.
- [7] Anne Mergy, Guran Lecuyer, Dawa Derksen, and Dario Izzo. Vision-based neural scene representations for spacecraft. *CVPR*, 2021.
- [8] Ben Mildenhall, Peter Hedman Ricardo, Martin-Brualla, Pratul P. Srinivasan, and Jonathan T. Barron. Nerf in the dark: High dynamic range view. *CVPR*, 2022.
- [9] Ben Mildenhall, Pratul P. Srinivasan, Matthew Tancik, Jonathan T. Barron, Ravi Ramamoorthi, and Ren Ng. Nerf: Representing scenes as neural radiance fields for view synthesis. *ECCV*, 2020.
- [10] Max Nelson. Optical models for direct volume rendering. *IEEE Transactions on Visualization and Computer Graphics*, 1995.
- [11] Jeong Joon Park, Peter Florence, Julian Straub, Richard Newcombe, and Steven Lovegrove. Deepsdf: Learning continuous signed distance functions for shape representation. *CVPR*, 2019.
- [12] Tae Ha Park, Marcus Märtens, Guran Lecuyer, Dario Izzo, and Simone D’Amico. Speed+: Next-generation dataset for spacecraft pose estimation across domain gap. *CVPR*, 2021.
- [13] Matt Pharr, Wenzel Jakob, and Greg Humphreys. *Physically based rendering: From theory to implementation*. 2023.
- [14] Katja Schwarz, Yiyi Liao, Michael Niemeyer, and Andreas Geiger. Graf: Generative radiance fields for 3d-aware image synthesis. *Advances in Neural Information Processing Systems*, 1970.
- [15] Luke Taylor and Geoff Nitschke. Improving deep learning using generic data augmentation. *IEEE symposium series on computational intelligence*, 2018.
- [16] Zirui Wang, Shangzhe Wu, Weidi Xie, Min Chen, and Victor Adrian Prisacariu. Nerf-: Neural radiance fields without known camera parameters. *CVPR*, 2022.

**DISTRIBUTION A. Approved for public release: distribution is unlimited.
Public Affairs release approval #AFRL-2023-378**

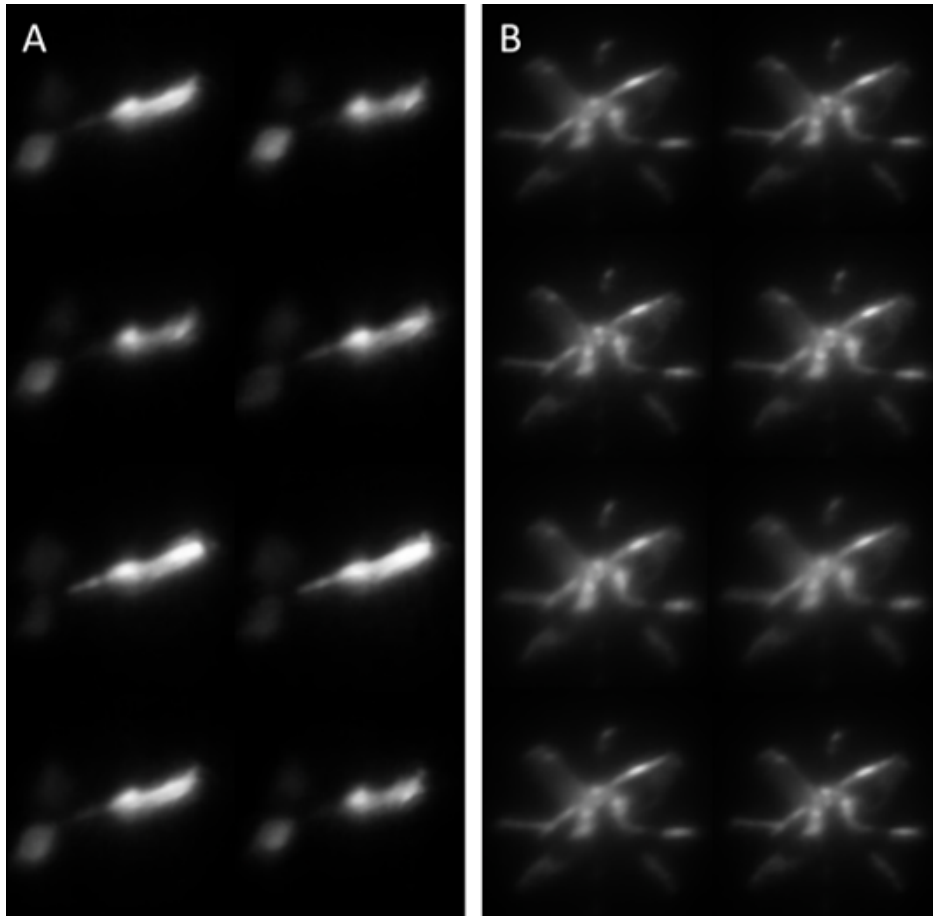


Fig. 13: Novel Views of 1.6 meter Real Satellite Images. A - NOAA 13. B - COSMOS 1606.

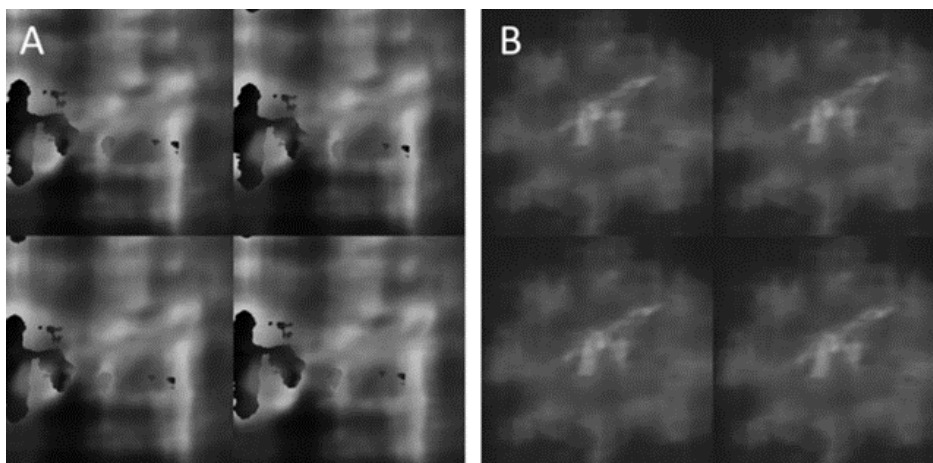


Fig. 14: Depth Maps of 1.6 meter Real Satellite Images. A - NOAA 13. B - COSMOS 1606.

DISTRIBUTION A. Approved for public release: distribution is unlimited.
Public Affairs release approval #AFRL-2023-378

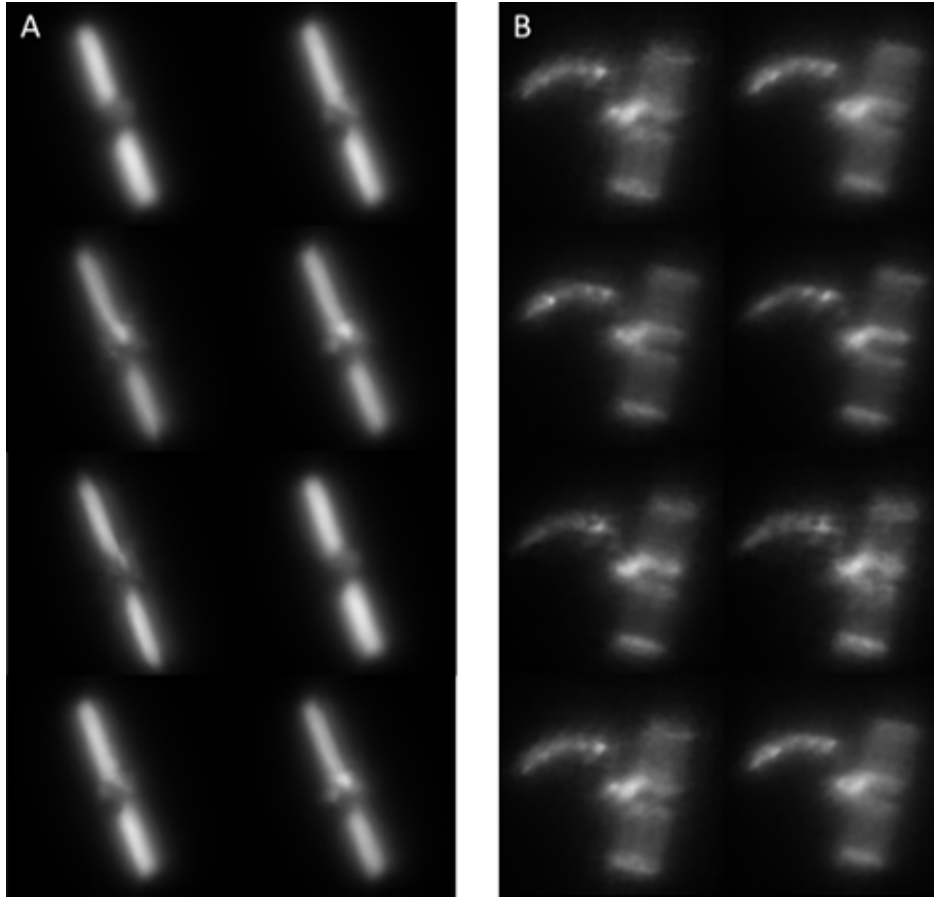


Fig. 15: Novel Views of 3.6m Real Satellite Images. A - RESURS O1. B - SPOT 2.

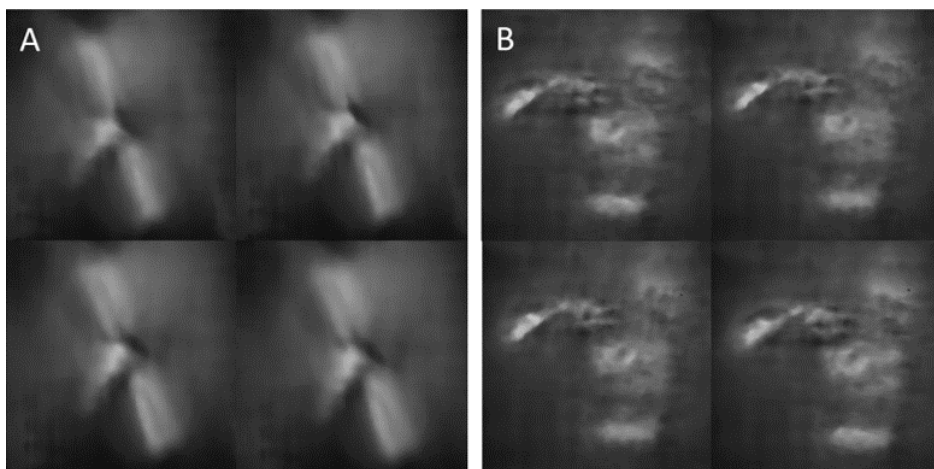


Fig. 16: Depth Maps of 3.6m Real Satellite Images. A - RESURS O1. B - SPOT 2.

DISTRIBUTION A. Approved for public release: distribution is unlimited.
Public Affairs release approval #AFRL-2023-378